Raman Chemical Imaging of Microcrystallinity in Silicon Semiconductor Devices

MICHAEL D. SCHAEBERLE, DAVID D. TUSCHEL, and PATRICK J. TREADO*

National Institutes of Health, Building 5, Room B1-38, Bethesda, Maryland 20892 (M.D.S.); Imaging Research and Advanced Development, Eastman Kodak Company, Rochester, New York 14650-2132 (D.D.T.); and ChemIcon Inc., 7301 Penn Avenue, Pittsburgh, Pennsylvania 15208 (P.J.T.)

Silicon integrated circuits are fabricated by the creation of complex layered structures. The complexity of these structures provides many opportunities for impurities, improperly annealed dopants, and stress effects to cause device contamination and failure. Nondestructive metrology techniques that rapidly and noninvasively screen for defects and relate silicon device structure to device performance are of value. We describe the first use of a liquid crystal tunable filter (LCTF) Raman chemical imaging microscope to assess the crystallinity of silicon semiconductor integrated circuits in a rapid and nondestructive manner without the need for sample preparation. The instrument has demonstrated lateral spatial resolving power of better than 250 nm and is equipped with a tunable imaging spectrometer having a spectral bandpass of 7.6 cm^{-1}. The instrument rapidly produces high-definition Raman images where each image pixel contains a high-quality Raman spectrum. When combined with powerful processing strategies, the Raman chemical imaging system has demonstrated spectral resolving power of 0.03 cm^{-1} in a test silicon semiconductor wafer fabricated by using ion implantation. In addition, we have applied Raman chemical imaging for volumetric Raman imaging by analyzing the surface distribution of polycrystalline thin film structures. The approaches described here for the first time are generally applicable to the nondestructive metrology of silicon and compound semiconductor devices.

Index Headings: **Silicon semiconductors; Ion implantation; Polysilicon; Chemical imaging; Raman imaging; Raman spectroscopy; Volumetric imaging; Numerical confocal microscopy.**

INTRODUCTION

Silicon-based integrated circuits (ICs) are used in everything from scientific-grade digital charge-coupled device (CCD) detectors to personal computers to automatic drip coffee makers. Integrated circuits require the fabrication of complex three-dimensional layered structures using multi-step processes including ion implantation and thermal annealing. The electronic performance of layered silicon devices can be compromised at any number of stages during the manufacturing process. For example, impurities in the initial semiconductor starting material, incomplete annealing of ion implantation sites, changes in microcrystallinity, and strain can all lead to device failure.[1]

Careful control of device fabrication to meet engineering specifications is critical. Nondestructive metrology techniques that can rapidly measure IC device characteristics, including chemical composition, crystalline structure, and three-dimensional (volumetric) architecture are highly desirable, but not widely available. It is recognized that new analytical techniques are needed to assist IC device research and development as critical dimensions get smaller and new materials are evaluated for incorporation into ICs.[2]

Failure analysis methods are also needed that can characterize the physical morphology and chemical composition of defective semiconductor devices. Analytical data collected from the defective regions are compared with those of a standard working device; morphological and chemical differences between the two can be used to diagnose the cause of the failure.

One area where nondestructive metrology is essential is in support of routine quality monitoring within fabrication facilities. One opportunity for cost reduction in device fabrication is through more effective screening of defects at intermediate processing steps that can reject devices that are likely to fail. Where feasible, automated inspection is also desirable in manufacturing environments that are touch-labor intensive. Similarly, by understanding how chemical and morphological changes affect performance in normal devices, manufacturers can produce products with specific or improved properties. Methods that can relate changes in a sample's morphological and chemical composition to its performance are of increasing importance in the semiconductor industry.

Raman spectroscopy is an established analytical technique for characterizing semiconductor properties.[3–5] It has been used to assess semiconductor quality on the basis of the crystallinity of the semiconductor,[4,5] the presence of structural damage within a device,[6] the damage induced by ion implantation,[7–10] the distribution of impurities,[11] the effect of thermal annealing,[12] and the extent of stress.[13–16]

With the introduction of the Raman microprobe in 1975,[17] measurements of silicon semiconductor lattice properties on spatial dimensions relevant to miniaturized ICs became possible. However, the Raman microprobe is limited to providing microscale spectral information from isolated spatial locations. In order to image the spatial distribution of microstructures, the Raman microprobe has limited ability to probe surfaces in an efficient manner.

To address the inherent inefficiency of the Raman microprobe as a spatial mapping instrument, a variety of Raman chemical imaging instruments based on scanning,[17,18] spatial multiplexing,[19] and tunable filter[20–23] approaches have been developed. Raman imaging instruments combine Raman spectroscopy and digital imaging technology to generate chemical composition and/or structure specific image contrast. Contrast is derived from

Received 6 July 2000; accepted 27 November 2000.
* Author to whom correspondence should be sent.

0003-7028/01/5503-0257$2.00/0

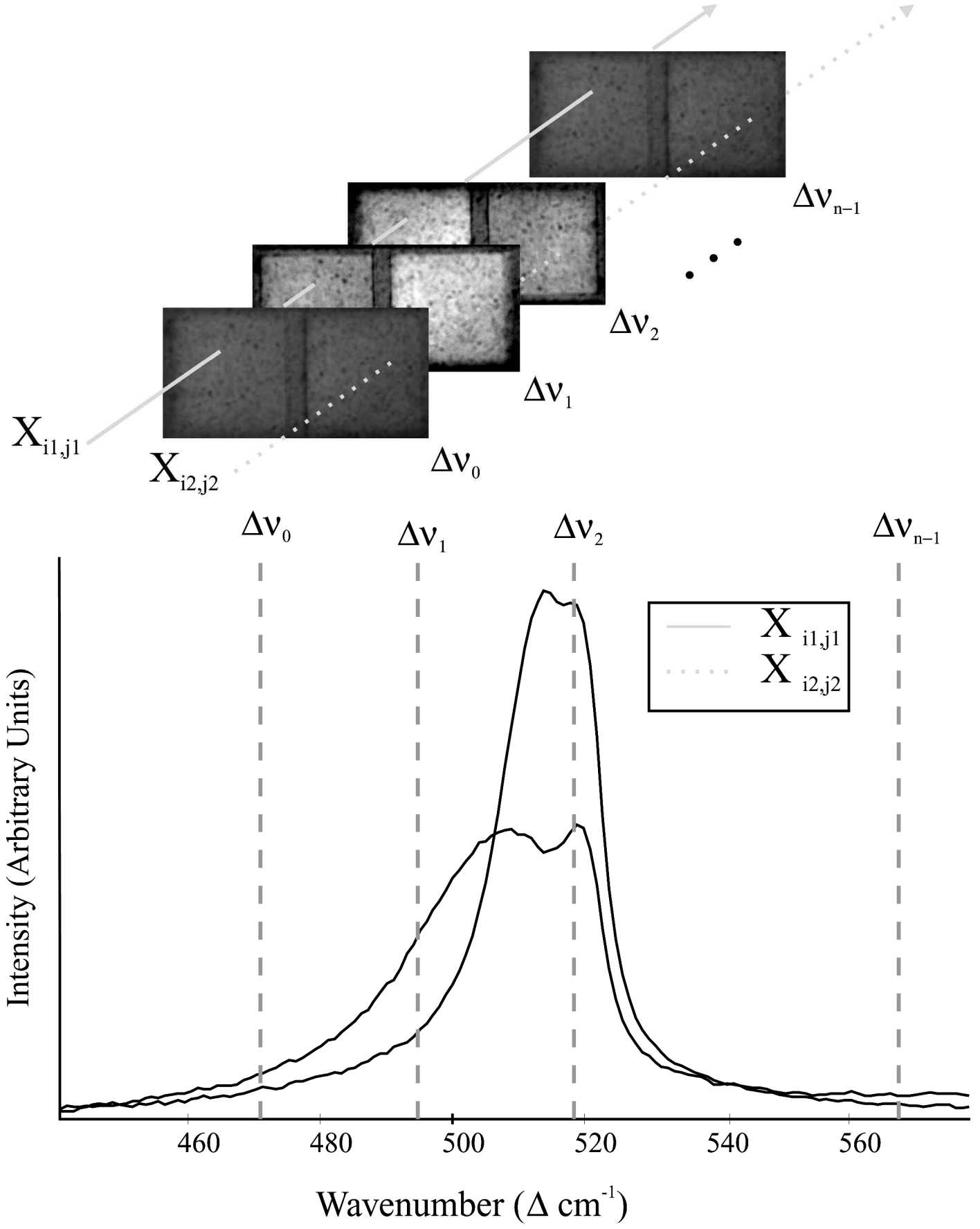

FIG. 1. Raman chemical imaging data sets comprise multiple dimensions of information, including two (or three) spatial dimensions and one spectral dimension. The image describes sample morphology (top), while each point in the image is a complete Raman spectrum (bottom), which describes sample chemistry.

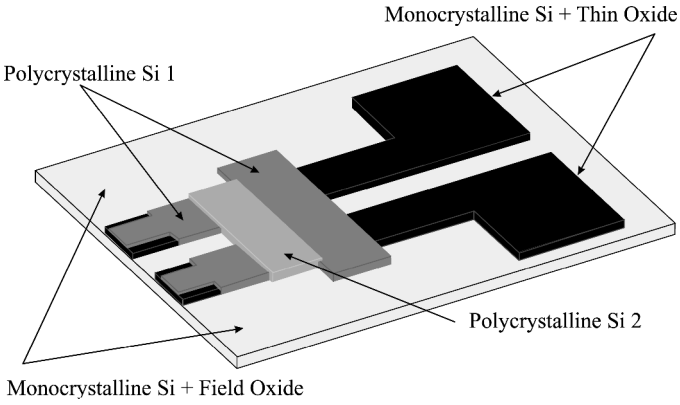

FIG. 2. Diagram of the surface test structure on a monocrystalline silicon integrated circuit wafer.

spatially resolved Raman spectra, which reveal a semiconductor's chemical bonding and atomic order. Further, Raman chemical imaging is proving to be an attractive technique for semiconductor analysis because images can be generated rapidly and noninvasively on the basis of the intrinsic scattering properties of the lattice without the need for contrast agents or sample preparation.

Microcrystalline, polycrystalline, and single-crystalline silicon are important building blocks in the construction of semiconductor device architectures. Silicon crystallinity can be characterized by probing for differences in the Raman peak at 520.2 cm^{-1}, which arise from the triply degenerate, first-order optical phonon mode. Peak shifts and broadening can reveal information on the microcrystalline grain size and distribution thereof, but these spectral changes can also be influenced by strain in the material.

Raman microscopy employing liquid crystal tunable filters (LCTFs) is widely recognized as the most efficient technological approach to Raman imaging.[24] Liquid crystal tunable filter Raman chemical imaging provides spatial information by globally illuminating the sample and by using a two-dimensional CCD to record the image. The spectral dimension is recorded by sequentially tuning the wavelength of the LCTF between image acquisitions. This procedure creates a three-dimensional (two spatial, one spectral) Raman chemical image cube, as illustrated in Fig. 1. The image cube can be conceptualized in two ways: (1) as a series of images recorded at discreet spectral bands; and (2) as a collection of spatially resolved Raman spectra. The duality of the data can be exploited by employing chemical image processing strategies to derive a greater amount of information than is available from a single image or spectrum alone.

In this paper, we describe the first use of an LCTF Raman chemical imaging system to study the chemical composition of a silicon semiconductor integrated circuit. The microcrystallinity of polycrystalline silicon and/or the presence of strain within the IC will be assessed by using image processing methods based on spectral intensity and peak band shape parameters, including center of mass (COM) and full width at half-maximum (FWHM). In addition we also describe the first extension of Raman chemical imaging to volumetric analysis. LCTF Raman chemical imaging is performed as a function of depth to characterize the three-dimensional (volumetric) distribution of polycrystalline Si and oxide thin films near the IC surface.

EXPERIMENTAL

The LCTF Raman chemical imaging system has been described previously.[20,25,26] Briefly, an argon-ion laser operating at 514.5 nm (Lexel 150) is coupled either directly

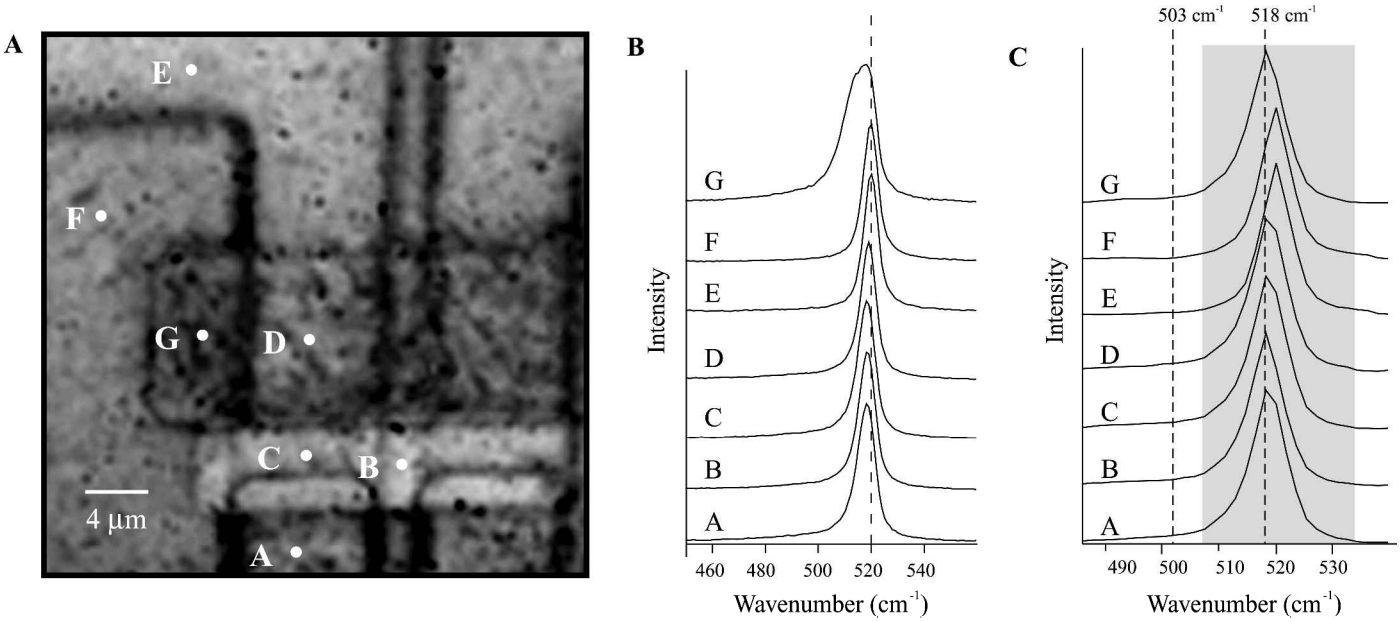

FIG. 3. Raman microspectra of silicon IC test structure. (**A**) Reflectance brightfield image of test structure collected with a 50× (NA = 0.80) objective. Points labeled in the image correspond to microspectra collected by using dispersive Raman (**B**) and LCTF Raman (**C**). The two Raman spectrometers reveal consistent variability across the test structure showing deviations from unstrained monocrystalline silicon (520.2 cm^{-1}). The dotted lines in **C** represent positions for on-peak (518 cm^{-1}) and background (503 cm^{-1}) regions for ratiometric image processing shown in Fig. 5. The shaded box shows the spectral range (507–534 cm^{-1}) that was employed for COM and FWHM image processing shown in Fig. 5.

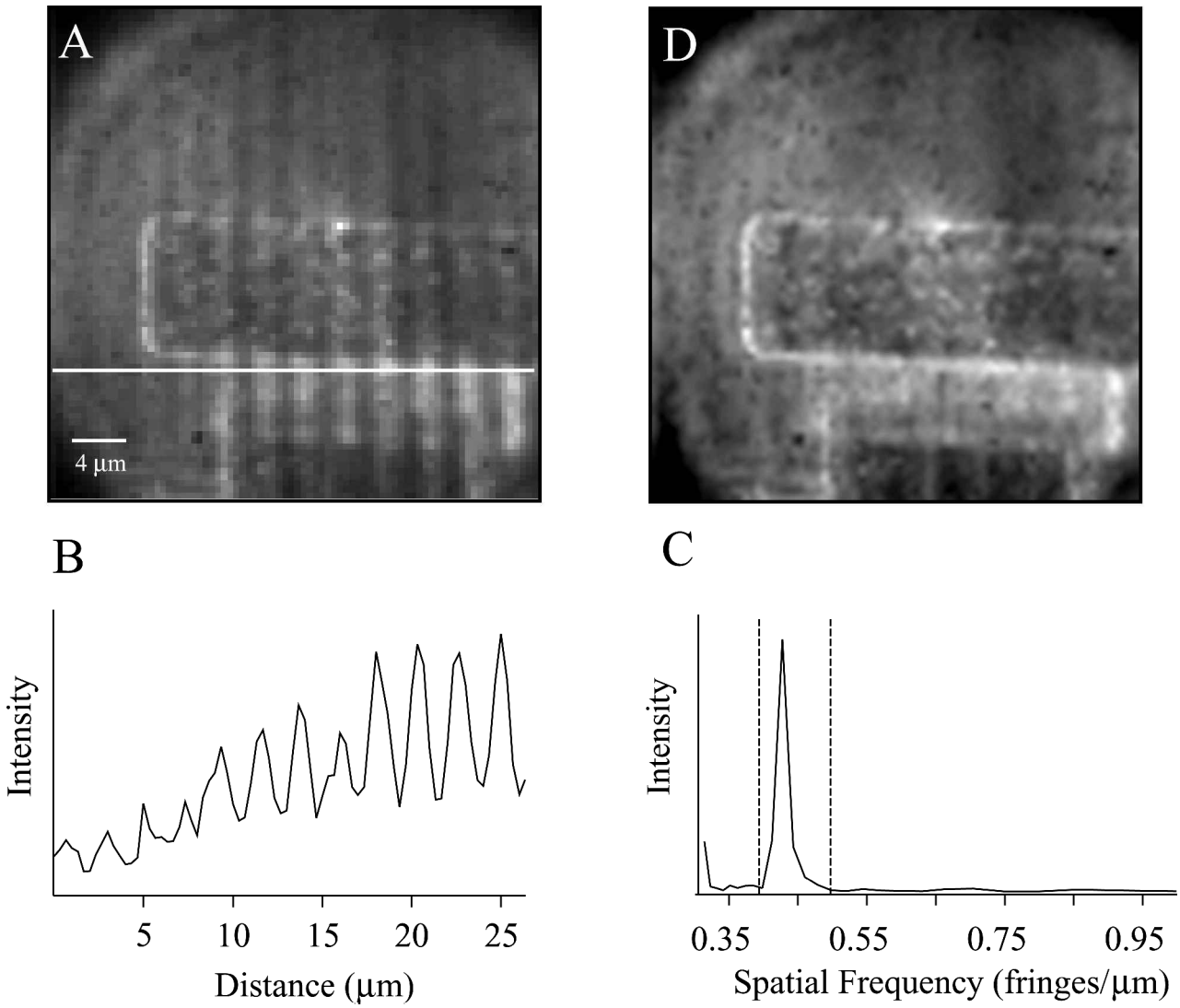

FIG. 4. Fast Fourier transform image processing to suppress interference fringes from Raman intensity images. (**A**) Raw Raman image collected at 518 cm^{-1} showing the interference fringes. (**B**) Line intensity profile corresponding to white line in 4A. (**C**) Power spectrum of line profile showing spatial frequencies responsible for the interference fringes. (**D**) Inverse FFT image with interference fringes minimized.

or via a fiber optic (CeramOptic) to an optical microscope (Olympus B-H2) for sample excitation. Raman scattered radiation is collected by an infinity-corrected objective and is presented to holographic notch rejection filters (Kaiser Optical), which reject the Rayleigh light and pass the Raman image. For nonimaging microspectral analysis, a mirror directs the Raman scatter to a remote spectrometer (Chromex 500IS) via a focusing lens (Oriel) and a Raman emission fiber optic (CeramOptic). In imaging mode, the Raman light is presented to a high-resolution LCTF (Cambridge Research & Instrumentation) for Raman bandpass filtering. Relay optics focus the filtered image onto a back-thinned, high-dynamic-range CCD detector (Princeton Instruments, TEK512B).

Pentium-based personal computers are used for Raman image collection and processing. Image acquisition and LCTF control are provided by using a macro developed for use in a commercial software package (Princeton Instruments, WinView 1.6). Chemical image visualization and processing are performed by using routines written for the Matlab software environment (Mathworks). For presentation, images are printed on a dye sublimation printer (Tektronix, Phaser 450).

Raman microprobe spectroscopy and chemical imaging were performed on a test pattern located on a silicon IC. The test pattern is shown schematically in Fig. 2 and contains single-crystal silicon with a thin oxide layer (~ 900 Å) and two forms of polycrystalline silicon deposited on a single-crystal silicon substrate that is covered by a field oxide layer (~ 8500 Å). The silicon IC was examined with LCTF Raman chemical imaging to distinguish different structural forms of silicon, including single crystalline material vs. polycrystalline material, as well as to visualize the stress associated with device features, including oxide growth films.

RESULTS AND DISCUSSION

A brightfield reflectance image of the test pattern is shown in Fig. 3A. Although device morphology is discernible in the image due to interference color differences between the device structures having different thickness-

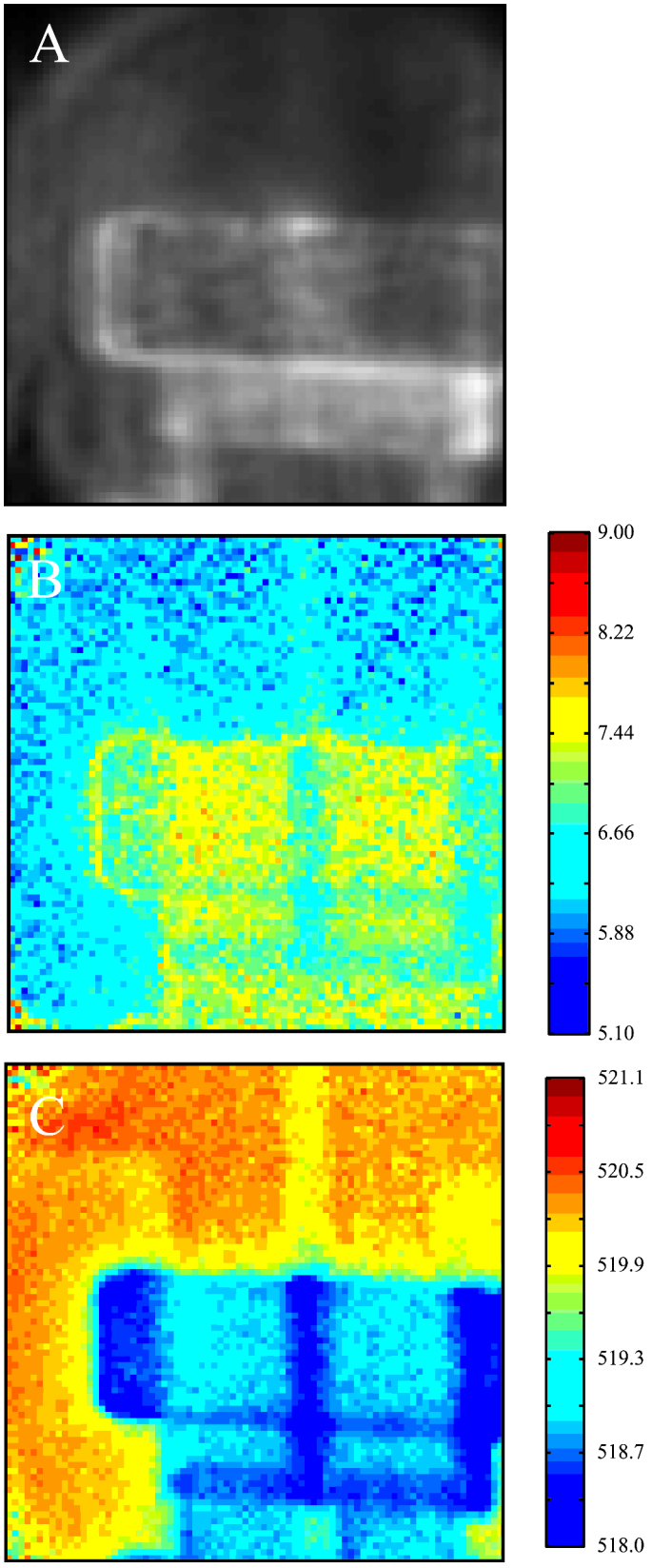

FIG. 5. (**A**) Ratiometric Raman image (518 cm^{-1}/503 cm^{-1}). (**B**) Bandwidth Raman image pseudo-colored to denote the FWHM value in wavenumbers. (**C**) Band center of mass (COM) Raman image pseudo-colored to denote peak position in wavenumbers.

es, it is not possible to assess the degree of crystallinity or strain by using conventional brightfield microscopy alone.

Brightfield microscopy, when used in conjunction with Raman microprobing, can support survey assessments to identify heterogeneities in grain size and strain distributions of the polycrystalline structures in the test pattern. Conventional dispersive Raman microspectra of the silicon test pattern were collected by operating the microscope in microprobe mode and using a 50× [0.80 numerical aperture (NA)] objective. The spectra shown in Fig. 3B, labeled to correspond to the sampling points in Fig. 3A, consist of Raman bands restricted by the backscattering arrangement to the first order longitudinal optical (LO) phonon mode. Spectrum F, acquired from the silicon substrate, serves as the reference for unstrained single crystal silicon. The peak maximum of the reference spectrum is located at 520.2 cm^{-1} and is represented by the dotted line in Fig. 3B. The presence of peak shifts and band broadening, relative to spectrum F, provides evidence for the existence of sample heterogeneity, which can be indicative of changes in the degree of crystallinity (i.e., grain size distribution) or the degree and orientation of stress experienced by each structure. Raman microprobe analysis confirms the heterogeneous nature of the sample, but does not provide good sampling statistics on the heterogeneity distribution. As a result, a detailed understanding of crystallinity architecture within the test pattern cannot initially be obtained through Raman microprobe analysis alone. However, the interpretation of Raman spectra, as they relate to strain and grain size, can be established through a correlation to the results of transmission electron microscopy performed on these materials.

LCTF Raman chemical imaging provides a more comprehensive analysis than the Raman microprobe for measuring the distribution of silicon crystallinity and stress within the integrated circuit test pattern. Normalized LCTF Raman spectra from the three-dimensional image data sample are shown in Fig. 3C and are plotted from the same locations sampled via the Raman microprobe. Again, spectrum F corresponds to unstrained single-crystal silicon. Peak shifts and band broadening can be observed in the LCTF spectra that are consistent with the Raman microprobe data. In the LCTF data set, 6400 spectra are collected in less than 14 min.

A representative raw Raman image from the LCTF data set at 520 cm^{-1} is shown in Fig. 4A. An interference pattern can be seen in the image. This pattern degrades the image quality and arises from the holographic notch filters (HNFs) when they are operated off their design angle. These filters were designed to be operated at normal (0°) incidence. However, in this prototype instrument configuration they are operated at 11° off-axis. Employing holographic filters optimized for the operating angle eliminates the interference.

As an alternative to modifying the optical design in order to minimize the contribution of the interference, we have employed Fourier transform digital image processing. The approach is illustrated in Fig. 4 for a single row of the image. However, in the analysis all rows are treated simultaneously. Figure 4B shows a line profile for a single row of the image in which the sinusoidal periodicity

of the interference fringes can be observed. A fast Fourier transform (FFT) is applied to the line profile to transform the data into frequency space and identify spatial frequencies responsible for the interference pattern, as seen in Fig. 4C. The responsible spatial frequencies are zero-filled to remove the interference pattern's contribution to the image, and an inverse FFT is performed on the processed spatial frequency data to recover an image with minimal interference, as seen in Fig. 4D. This method is adequate for improving the appearance of the image and performing the analysis discussed in this paper, but does have its limitations. With zero-filling, the interference is minimized, but the approach imposes a degree of coherence with respect to the spatial frequencies.

Spatial dimension image processing improves Raman image contrast. However, spectral dimension processing is even more effective. Spectral ratiometric image processing is one of the simplest techniques used to generate and enhance image contrast. Raman images at specific spectral band positions are divided by a background Raman image to suppress instrument response such as nonuniform illumination. For example, Fig. 5A shows the ratio of Raman images at 518 cm^{-1} (indicative of polycrystalline Si) by 503 cm^{-1} (background). The resulting ratiometric Raman image highlights the polycrystalline silicon regions. Because the spectral differences between the polycrystalline and single-crystal silicon are slight, with peak position differences often <2 cm^{-1}, ratiometric analysis is generally ineffective for component differentiation. Strategies that employ more of the spectrum have proven to be more effective.[26] The key is to gather and process enough of the spectrum but not too much because of tradeoffs between specificity and speed. For example, univariate approaches are particularly effective for semiconductors because of relatively simple spectra encountered in monolithic materials. Changes in silicon lattice properties are often manifested as subtle changes in peak position and peak width. These band shapes are characterized by center of mass and full width at half maximum parameters. Unlike ratiometric techniques, which use only one or two images at specific wavelengths, band shape methods make use of the abundant information present in the Raman spectrum that is available at each pixel in the image. The analysis produces a new image based solely on a band shape parameter and is intensity independent, as long as a significant signal-to-background ratio is achieved. The new image is created by calculating the FWHM or COM of the Raman spectrum at each pixel and placing that value in the corresponding position in the new image. Images based on the FWHM and COM can be calculated from the raw data without data pretreatment (i.e., no FFT filtering) by examining the offset-corrected Raman spectral region from 507 to 534 cm^{-1}. Limiting the analysis to this region minimizes the effect small fluctuations in the background baseline have on the calculated FWHM or COM value.

An image based on FWHM analysis is shown in Fig. 5B. Three distinct regions, corresponding to measured peak widths of approximately 6.1, 6.8, and 7.4 cm^{-1}, can be clearly observed in the image. The smallest peak width corresponds to the single-crystal silicon, while the largest peak width is associated with polycrystalline silicon. We note that the measured peak widths are broader than the natural linewidths. For example, the natural linewidth of single-crystal silicon is 3 cm^{-1}. The measured broadening is due, in part, to the bandpass of the LCTF imaging spectrometer. While the LCTF contributes broadening to the measured bandwidth, it can still differentiate subtle changes in the peak width and peak position. The 6.8 cm^{-1} peak width appears to occur mainly where the polycrystalline silicon overlaps the single-crystal silicon substrate and may indicate a change in the crystalline grain size, or the distribution of strain, or a combination of both in these regions. Although the structures visible in FWHM image are similar to those seen in the ratiometric image in Fig. 5A, the FWHM image provides quantitative parameters that relate to the degree of crystallinity and strain while the ratiometric image does not. While the FWHM image provides information on the degree of crystallinity/strain in the silicon test pattern, it does not reveal the subtlest features in the sample. A more powerful approach is shown in Fig. 5C in which the peak COM is analyzed at each pixel location to discriminate subtle spectral shifts. The COM image is not only able to distinguish the major features of the test pattern, with the polycrystalline regions (blue) clearly differentiated from the single-crystal silicon regions (red/orange), but also reveals more subtle features that are not readily apparent in either the ratiometric or FWHM images, including the yellow region that seems to border all the structures. The Raman bands from this region are, as expected from microcrystalline silicon, shifted to lower energy and broadened relative to the 520.2 cm^{-1} band of the single-crystal silicon substrate. Therefore, it seems likely that the band broadening and shift to lower energy arise from strain at the substrate/structure interface.

More surprisingly, single-crystal silicon with different oxide layer thickness, labeled regions 1 and 2 in the inset image in Fig. 6, is also observable in the COM image. A graph of the mean COM and standard deviation for all of the areas labeled in the image shows that the two single-crystal silicon structures differ in their mean COM by only 0.03 cm^{-1}. The statistical significance of the shifts seen in the COM image is analyzed by a *t*-test comparison of two experimental means.[27] The mean COM, standard deviation of the mean, populations, and calculated *t* values for regions whose mean COMs are within one standard deviation are tabulated in Table I. Comparing calculated *t*-values to literature values found in standard statistical tables,[27] it can be seen that in all cases, except when comparing regions 6 and 8, the difference in the means is statistically significant at the 99.9% confidence interval. For regions 6 and 8, no statistically significant difference between the two forms of polycrystalline silicon can be seen, although both regions do have statistically different mean COMs from the other polycrystalline regions (regions 4, 5, and 7). These differences are most likely due to a convolution of a change in microcrystalline grain size and a distribution of strain. By employing transmission electron microscopy, it would be possible to differentiate and quantify grain size and strain distributions.

It is not expected that the polycrystalline Si device structures would exhibit different degrees of lattice order. The only differences in the layered materials are the stage in the fabrication process when they are patterned and their subsequently different thermal histories. It was ini-

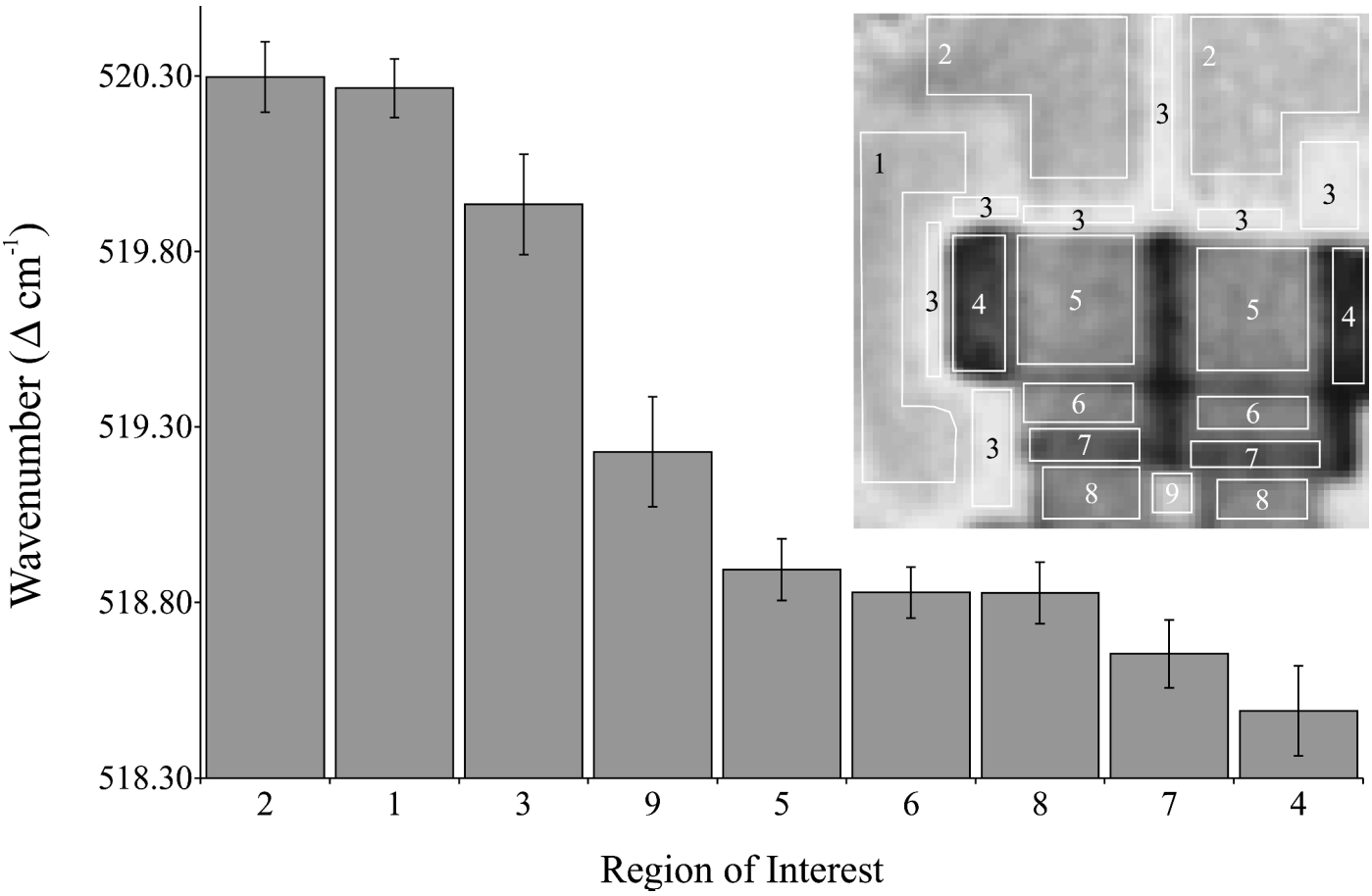

FIG. 6. Plot of the mean center of mass and standard deviation for each region labeled in the inset COM image. Region of interest selection is guided by image contrast and *a priori* knowledge about the test structure morphology.

tially surprising that regions 1 and 2, having a statistically significant difference in their mean COM of only 0.03 cm^{-1}, can be differentiated. However, these regions differ in their respective oxide layer thickness, which can impart different degrees of strain on the underlying silicon lattice. For example, strain-induced Raman shifts of 0.1 cm^{-1} or less that are similar to those we report in this study have been detected at the interface between crystalline Si and field oxide (SiO_2).[28] These findings are consistent with our work.

The spectral resolving power of the LCTF Raman chemical imaging system demonstrated here results from the excellent sampling statistics of the experiment. Unlike conventional mapping techniques that have relatively few sampling points, the large number of points in the LCTF Raman image data (6400) improves the confidence interval of the measurement by decreasing the standard error of the mean and improving the signal-to-noise ratio, both of which are dependent on the square root of the number of sampling points. The *t*-test confirmation that the mean COMs of regions 1 and 2 are statistically different shows that LCTF Raman chemical imaging with COM band shape analysis provides sensitivity to spectral peak shifts that are 253 times narrower than the LC imaging spectrometer bandpass.

The previous data have focused on two lateral spatial

TABLE I. Statistical comparison table for representative regions of interest (ROI) within the test structure. Most ROIs can be differentiated based on their Raman COMs to within a 99.9% confidence level by comparing the calculated *t*-value to the reference *t*-value (3.291). ROIs 6 and 7 do not exhibit statistically significant differences in COM.

Region no.	Mean COM	SD	No. of spectra	Region no.	Mean COM	SD	No. of spectra	Degrees of freedom	Calculated *t*-value
1	520.265	0.0839	716	2	520.297	0.1008	1273	1715	7.566
4	518.491	0.1279	346	5	518.594	0.0876	773	496	53.226
4	518.491	0.1279	346	6	518.829	0.0730	197	543	39.138
4	518.491	0.1279	346	7	518.654	0.0971	251	596	17.643
4	518.491	0.1279	346	8	518.827	0.0868	254	596	38.321
5	518.594	0.0876	773	6	518.829	0.0730	197	356	10.704
5	518.594	0.0876	773	8	518.827	0.0868	254	436	10.554
6	518.829	0.0730	197	7	518.654	0.0971	251	447	21.766
6	518.829	0.0730	197	8	518.827	0.0868	254	448	0.174
7	518.654	0.0971	251	8	518.827	0.0868	254	497	21.182

dimensions and have neglected the depth spatial dimension. It is important to realize that in a widefield Raman imaging experiment, this third spatial dimension can have a profound influence on the spectrum of a structure being probed since the penetration depth of the laser is not restricted to a single focal plane, as in any optical microscope. For example, the schematic diagram of the silicon test pattern illustrates the three-dimensional structure of the layered device. The Raman chemical imaging system described here provides a means to image three-dimensional structures rapidly and noninvasively without cross-sectioning the sample. Volumetric Raman chemical images were generated by fixing the focal plane of the microscope at a range of focal depths and collecting Raman chemical images at each focal plane. Figure 7A shows a volumetric image composed of a series of six FFT corrected images collected at 518 cm^{-1}, by adjusting the focal position of the sample in 0.53 μm increments.

In performing volumetric imaging of silicon using visible laser excitation, the depth of penetration of the laser should be considered. At 514.5 nm, the absorptivity of crystalline Si is 15 080 cm^{-1} and depth of penetration is 762 nm.[29] The features that dominate the images of Fig. 7 are polysilicon layers that are only several hundred nanometers thick. As a result of polysilicon's increased transparency, relative to crystalline Si, and the fact that the polysilicon layers are so thin, the Raman imaging focal plane can readily interrogate from the top of the polysilicon to the crystalline Si substrate. Because the laser source does not penetrate deep into the underlying substrate, the focal plane discrimination is effectively enhanced.

The ability to generate chemically meaningful volumetric images requires that contributions from out-of-focus planes be minimized. Nearest neighbor deblurring (NND) is a haze-subtraction algorithm that subtracts a weighted percentage of the intensity of the image planes above and below from the plane being analyzed. This is done for each FFT filtered image in the stack, except for the first and last image planes, which are discarded. The NDD volumetric image is shown in Fig. 7B and was generated from eight initial image planes so that the processed result is comparable to that in Fig. 7A. Significant improvements in the deblurred volume image contrast can be observed relative to the blurred volume image despite the simplicity of the NND algorithm relative to more rigorous deconvolution approaches.[30–32]

Figures 7A and 7B are constructed from Raman images captured at a constant spectral band and provide minimal insight into how microcrystallinity changes as a function of depth. As we have shown, variations in crystallinity and strain can be revealed by band COM analysis. By calculating a COM image for each focal plane, one can create a volumetric COM image, shown in Fig.

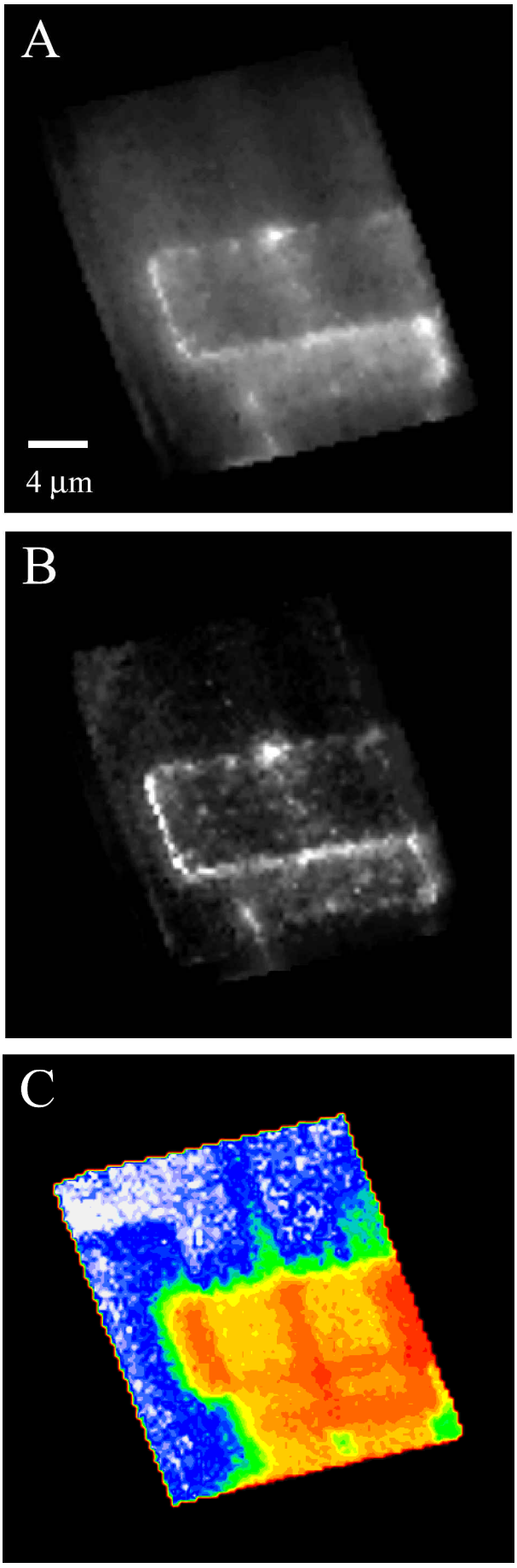

→

FIG. 7. Volumetric Raman chemical imaging. (**A**) Volumetric image collected at 518 cm^{-1}. Image blur is visible. (**B**) De-blurred volumetric Raman image using nearest neighbor deblurring algorithm applied to fringe-suppressed intensity images. (**C**) Volumetric Raman chemical imaging reconstructed from axial-resolved COM images.

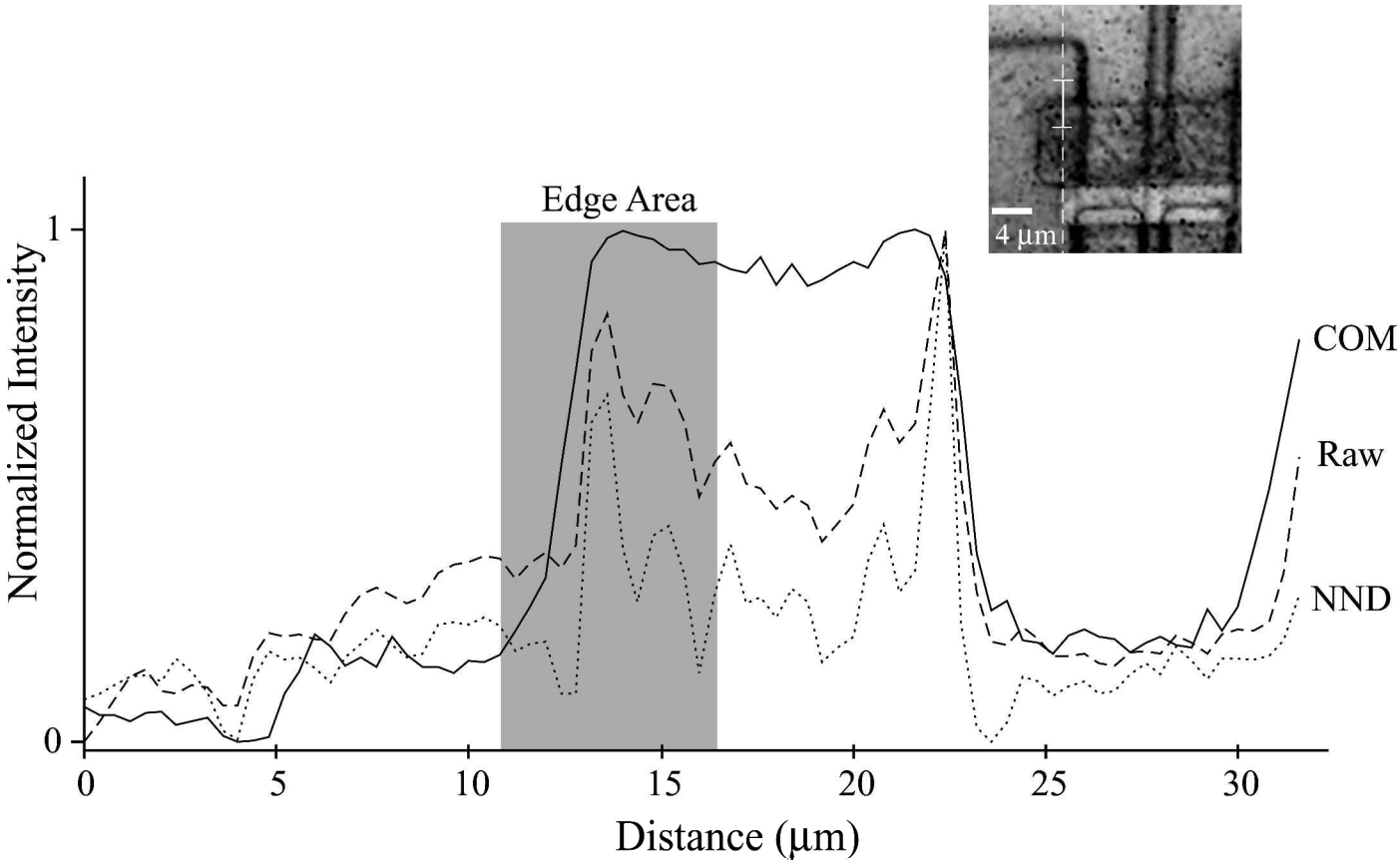

FIG. 8. Line profiles extracted along the dotted line shown in the brightfield image. The in-focus image of each volumetric image stack was analyzed for improvement in edge contrast in the area denoted by the solid line in the image and the shaded box in the plot.

7C. The image distinguishes microcrystalline from polycrystalline silicon, as a function of sample depth.

We have explored a quantitative method that goes beyond visual assessment to more objectively evaluate the performance of different volumetric processing methods. By monitoring edge response, it is possible to determine how the volumetric image processing methods affect the enhancement of Raman contrast in the silicon IC test pattern system. The in-focus image plane was selected for both the FFT filtered raw and NND stacks for analysis. The analysis consisted of extracting line profiles from the representative images, which are shown in Fig. 8. The line profiles were extracted along the dotted line shown in the brightfield image and are concentrated on the area around the boundary separating the substrate single crystal and the polycrystalline silicon.

A simple and effective evaluation of edge response involves calculating the first derivative of the boundary of interest.[33] The edge response is defined in Eq. 1, where $d(\mathrm{EP})$ is the derivative of the edge profile and $I_{\max}$ is the average maximum intensity along the boundary region and is used as a normalization factor.

$$\% \text{ edge contrast} = \left(\frac{d(\mathrm{EP})}{I_{\max}}\right) \times 100 \qquad (1)$$

A comparison of the percent contrast between the FFT filtered raw and NND images shows that a modest 0.67% improvement relative to the FFT filtered raw images is realized by employing the NND algorithm. This modest improvement can be perceived visually. Similar to the FFT corrected raw and NND volumetric stacks, a line profile was extracted from the COM in-focus image plane and is shown in Fig. 8. A substantial (41.4%) contrast improvement relative to the FFT corrected raw image can be measured.

CONCLUSION

LCTF Raman chemical imaging has demonstrated capacity for routine characterization and failure analysis of semiconductor devices by visualizing the spatial distribution of lattice microcrystallinity and strain in two and three spatial dimensions. By applying COM analysis to Raman chemical image data, we have demonstrated a 253× enhancement in spectral resolving power relative to the nominal spectral bandpass of the instrument. This enhancement corresponds to an observable spectral difference of 0.03 cm^{-1}. The enhanced spectral sensitivity allows LCTF Raman chemical imaging to identify extremely subtle spectral differences attributable to lattice disorder and strain. This capability suggests the possibility that Raman chemical imaging can provide a nondestructive means for high throughput screening of defects in Si ICs. This method has tremendous potential as the basis of a noncontact, in-process semiconductor metrology tool.

ACKNOWLEDGMENT

The authors wish to acknowledge partial financial support for M.D.S. through a grant from Eastman Kodak Company.

1. *Handbook of Semiconductor Silicon Technology,* W. C. O'Mara, R. B. Herring, and L. P. Hunt, Eds. (Noyes, Norwich, 1990).
2. International Technology Roadmap for Semiconductors, SEMATECH, Austin, Texas (1999).
3. *Light Scattering in Solids,* M. Cardona, Ed. (Springer, Berlin, 1983–1992), Vol. 1–6.
4. S. Perkowitz, *Optical Characterization of Semiconductors: Infrared, Raman, and Photoluminescence Spectroscopy* (Academic Press, London, 1993), Chap. 6.
5. F. H. Pollak, in *Analytical Raman Spectroscopy,* J. G. Grasselli and B. J. Bulkin, Eds. (John Wiley and Sons, New York, 1991), Chap. 6.
6. P. D. Wang, C. Cheng, C. M. Sotomayor-Torres, and D. N. Batchelder, J. Appl. Phys. **74,** 5907 (1993).
7. D. Kirillov, R. A. Powell, and D. T. Hodul, J. Appl. Phys. **58,** 2174 (1985).
8. A. C. deWilton, M. Simard-Normandin, and P. T. T. Wong, J. Electrochem. Soc. **1333,** 988 (1986).
9. G. Braunstein, D. Tuschel, S. Chen, and S. T. Lee, J. Appl. Phys. **66,** 3515 (1989).
10. U. V. Desnica, I. D. Desnica-Frankovic, M. Ivanda, K. Furic, and T. E. Haynes, Phys. Rev. B **55,** 16205 (1997).
11. F. A. Ponce, J. W. Steeds, C. D. Dyer, and G. D. Pitt, Appl. Phys. Lett. **69,** 2650 (1996).
12. K. Mizoguchi, Y. Yamauchi, H. Haruma, S. Nakashima, T. Ipposhi, and Y. Inoue, J. Appl. Phys. **78,** 3357 (1995).
13. M. Bowden, G. D. Dickson, D. J. Gardiner, and D. J. Wood, Appl. Spectrosc. **44,** 1679 (1990).
14. H. Miura, H. Ohta, H. Sakata, and N. Okamoto, JSME International Journal Series A **36,** 302 (1993).
15. K. Ajito, J. P. H. Sukamto, L. A. Nagahara, K. Hashimoto, and A. Fujishima, J. Vac. Sci. Technol., A **13,** 1234 (1995).
16. M. Bowden and D. J. Gardiner, Appl. Spectrosc. **51,** 1405 (1997).
17. M. Delhaye and P. Dhamelincourt, J. Raman Spectrosc. **3,** 33 (1975).
18. M. Bowden, D. J. Gardiner, G. Rice, and D. L. Gerrard, J. Raman Spectrosc. **21,** 37 (1990).
19. P. J. Treado, A. Govil, M. D. Morris, K. D. Sternitzke, and R. L. McCreery, Appl. Spectrosc. **44,** 1270 (1990).
20. H. R. Morris, C. C. Hoyt, P. Miller, and P. J. Treado, Appl. Spectrosc. **50,** 805 (1996).
21. G. J. Pupples, M. Grond, and J. Greve, Appl. Spectrosc. **47,** 1256 (1993).
22. D. N. Batchelder, C. Cheng, and G. D. Pitt, Adv. Mater. **3,** 566 (1991).
23. P. J. Treado, I. W. Levin, and E. N. Lewis, Appl. Spectrosc. **46,** 1211 (1992).
24. M. D. Schaeberle, H. R. Morris, J. F. Turner, and P. J. Treado, Anal. Chem. **71,** 175A (1999).
25. J. F. Turner and P. J. Treado, Proc. SPIE-Int. Soc Opt. Eng. **3061,** 280 (1997).
26. H. R. Morris, J. F. Turner, B. Munro, R. A. Ryntz, and P. J. Treado, Langmuir **15,** 2961 (1999).
27. C. Spatz, *Basic Statistics: Tales of Distributions* (Brooks/Cole, Pacific Grove, California, 1993), 5th ed., p. 353.
28. I. De Wolf, J. Raman Spectrosc. **30,** 877 (1999).
29. *Raman and Luminescence Spectroscopy of Microelectronics: Catalogue of Optical and Physical Parameters, ''Nostradamus'' Project SMT4-CT-2024* (European Commission, Science, Research and Development, Luxembourg, 1998), p. 20.
30. Q. S. Hanley, P. J. Verveer, T. and M. Jovin, Appl. Spectrosc. **52,** 783 (1998).
31. K. C. Carter, D. Bowman, W. Carrington, K. Fogarty, J. A. McNeil, F. S. Fay,and J. B. Lawrence, Science **259,** 1330 (1993).
32. D. A. Agard and J. W. Sedat, Nature **302,** 676 (1983).
33. N. J. Kline and P. J. Treado, J. Raman Spectrosc. **28,** 119 (1997).